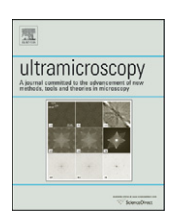
Contents lists available at ScienceDirect

Ultramicroscopy

journal homepage: www.elsevier.com/locate/ultramic



Dark-field electron holography for the measurement of geometric phase

M.J. Hÿtch*, F. Houdellier, F. Hüe¹, E. Snoeck

CEMES-CNRS and Université de Toulouse, 29 rue Jeanne Marvig, F-31055 Toulouse, France

ARTICLE INFO

Article history Received 28 July 2010 Received in revised form 19 April 2011 Accepted 24 April 2011 Available online 30 April 2011

Keywords: Electron holography Dark-field electron holography Geometric phase Strain

ABSTRACT

The genesis, theoretical basis and practical application of the new electron holographic dark-field technique for mapping strain in nanostructures are presented. The development places geometric phase within a unified theoretical framework for phase measurements by electron holography. The total phase of the transmitted and diffracted beams is described as a sum of four contributions: crystalline, electrostatic, magnetic and geometric. Each contribution is outlined briefly and leads to the proposal to measure geometric phase by dark-field electron holography (DFEH). The experimental conditions, phase reconstruction and analysis are detailed for off-axis electron holography using examples from the field of semiconductors. A method for correcting for thickness variations will be proposed and demonstrated using the phase from the corresponding bright-field electron hologram.

© 2011 Elsevier B.V. All rights reserved.

1. Introduction

Electron holography has been used for an ever widening range of applications ever since its invention by Gabor [1]. In his original conception, the measurement of the phase of the wave front would allow the determination of the aberrations of the optical system, and hence their elimination. This objective has been pursued and perfected in the field of high-resolution off-axis electron holography [2,3]. In the medium-resolution variety, understood as the measurement of the phase of the transmitted beam with respect to the vacuum, electron holography has been used to confirm the existence of the phase change due to the magnetic vector potential [4]. The local in-plane projection of the magnetic field can thus be determined [5], which has led to the development of the methodology for the quantitative study of magnetic fields at the nanoscale [6,7] and direct comparisons with micromagnetics modelling [8,9]. Similarly, the phase changes due to slowly varying electrostatic fields have been studied by medium-resolution holography, from the measurement of mean inner potentials of materials [10], to the potential drop across p-n junctions [11], the mapping of dopant concentrations in semiconductors [12], and the electric fields around emitting tips [13]. Indeed, the combination of electron holography and electron tomography heralds an era of many new results [14,15]. The current state of the art can be found in a number of reviews [16,17,18] and the recent Hannes Lichte 65th birthday issue of Ultramicroscopy [19].

However, electron holography is not limited to the measurement of these phases, as we will show. Geometric phase can also be measured and quantified by electron holography [20,21] using the dark-field electron holography (DFEH) configuration [22]. The technique has opened up a new range of applications for measuring strain in crystalline materials, notably in the field of semiconductor devices and thin films [23-27].

Geometric phase had previously been measured primarily by high-resolution electron microscopy (HRTEM) [28]. Its influence on conventional diffraction contrast has been recognised since almost the origins of electron microscopy [29] and from a more formal point of view, it is related to Berry phase, also known as geometric phase [30]. In electron microscopy, however, geometric phase usually refers to the variation of the phase across the wave front and not in the direction of propagation. In retrospect, it is natural to think that geometric phase could be measured directly by electron holography.

Our first attempt to measure geometric phase with electron holography was to analyse high-resolution electron holograms (HREH) in a similar way to HRTEM images [31]. Unfortunately the benefits are limited with respect to the latter technique and led to the idea of measuring the geometric phase directly from the diffracted beam [20]. The dark-field off-axis electron holography configuration we used was, in fact, a rediscovery of previous work by Hanszen, which had been left largely forgotten [22]. Whilst offaxis electron holography is a particularly efficient and accepted means to determine phases, there is no reason that other holography schemes should not be explored, such as by using in-line holography in a follow up to our experiments [32]. Indeed, there are more than twenty holographic configurations, which can be pursued [33].

^{*} Corresponding author.

E-mail address: hytch@cemes.fr (M.J. Hÿtch).

¹ Present address: University of Cambridge, Department of Materials Science, Pembroke Street, Cambridge, UK.

The aim of this paper is to outline the theory that led to the idea of dark-field holography, to describe the experimental setup and conditions, and to identify the systematic and random errors, which can influence the accuracy and precision of the strain measurements. The theoretical development will lead to a proposal for correcting systematic errors due to thickness variations. Examples will be given to illustrate both the method and the application of corrections. Whilst the experiments are all carried out in the off-axis mode, the theory and analysis are general to the other configurations of electron holography. Indeed, the benefits of off-axis with respect to in-line holography are expected to be the same as for other applications of medium-resolution holography and are not specific to dark-field experiments. For a direct comparison, see for example Ref. [34].

2. Electron holography

The different configurations for off-axis electron holography that will be discussed in this paper are shown schematically in Fig. 1. Plane-wave illumination is formed from the highly localised source and directed towards the object. In the conventional setup (Fig. 1a) part of the electron wave passes through the specimen and the other part through the vacuum. These two beams are deflected with the aid of a tuneable electrostatic biprism, so that they overlap to create an interference pattern on the screen. The electron hologram then encodes the phase difference between the electron paths through the vacuum and through the specimen. These phase shifts can be due to the presence of magnetic fields, electrostatic fields (including the crystalline atomic potential) and, as we will show, displacement fields.

The electron wave passing to the left, ψ_L , and right, ψ_R , of the biprism will interfere to produce holographic fringes of intensity $|y_L|^{2}$.

$$\psi_{L} = a_{L}e^{i\phi_{L}}e^{2\pi i} \overrightarrow{k_{L}} \overrightarrow{r}$$

$$\psi_{R} = a_{R}e^{i\phi_{R}}e^{2\pi i} \overrightarrow{k_{R}} \overrightarrow{r}$$

$$|\psi|^{2} = |\psi_{L} + \psi_{R}|^{2} = a_{R}^{2} + a_{L}^{2} + 2a_{R}a_{L}\cos\{2\pi \overrightarrow{q_{c}} \cdot \overrightarrow{r} + \phi_{RL}\}$$
(1)

where $\overrightarrow{q_c} = \overrightarrow{k_R} - \overrightarrow{k_L}$ is known as the carrier frequency, and $\phi_{RL} = \phi_R - \phi_L$, the phase difference. The phase of the hologram can be extracted by one of the phase retrieval methods, such as

the Fourier transform method, assuming a particular carrier frequency.

Eq. (1) is only valid for a single electron and needs to be integrated over the many electrons forming the image during the exposure time. The finite size of the electron source will limit the spatial coherence of the illumination and hence diminish the fringe contrast. Instabilities of the biprism (position and potential) will likewise reduce the fringe contrast as will the modulation transfer function (MTF) of the detector. All these factors will reduce the precision of the phase measurements.

2.1. Phase contributions

In most descriptions of medium-resolution electron holography, only the phase change of the transmitted beam is considered. Here, we will interest ourselves with the phase changes of both the transmitted and the diffracted beams created by a crystalline specimen. In addition, we will consider that the crystal is non-uniform; though departures from the norm will be treated as a perturbation. The wave function of the fast electron at the exit surface the crystal, $\psi(\mathbf{r})$, can then be written in the following way:

$$\psi(\mathbf{r}) = \sum_{g} \psi_{g}(\mathbf{r}) e^{2\pi i \mathbf{g} \cdot \mathbf{r}} \tag{2}$$

where \mathbf{r} is in the xy-plane, conjugate with the image plane, and \mathbf{g} the reciprocal lattice vectors of the perfect, or "reference", crystal [35]. Forward momentum is implicit and \mathbf{g} also includes the transmitted beam. The imperfections of the crystal are treated entirely within the local Fourier components, $\psi_g(\mathbf{r})$, which have a local amplitude and phase:

$$\psi_g(\mathbf{r}) = a_g(\mathbf{r})e^{i\phi_g(\mathbf{r})} \tag{3}$$

corresponding to the complex amplitudes of the transmitted and diffracted beams as a function of position across the exit surface of the crystal [36]. The phases here refer uniquely to the phases of Fourier components in reciprocal space and not those of the wave function in real space. We choose to write these phases as having four components:

$$\phi_{g}(\mathbf{r}) = \phi_{g}^{G}(\mathbf{r}) + \phi_{g}^{C}(\mathbf{r}) + \phi_{g}^{M}(\mathbf{r}) + \phi_{g}^{E}(\mathbf{r})$$
(4)

where C refers to the crystalline lattice, M the magnetic contributions, E the electric fields and G the geometric phase [37]. This subdivision will always remain, to some extent, artificial since from a physical interaction standpoint, there are only two sources

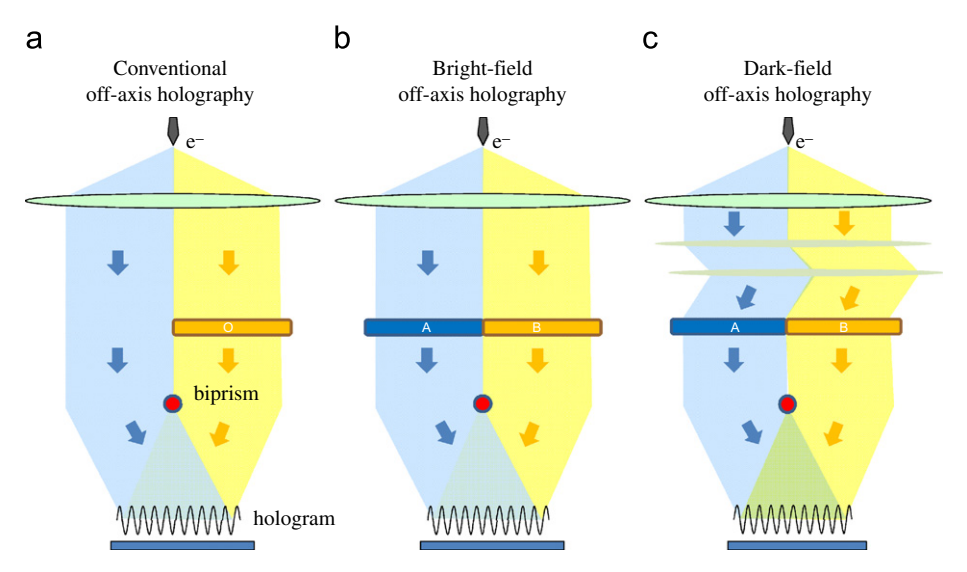


Fig. 1. Off-axis electron holography schemes: (a) conventional setup with specimen (O) and reference (vacuum); (b) bright-field holography with crystal (B) and reference crystal (A); (c) dark-field holography with strained crystal (B) and unstrained crystal (A).

for phase changes: electrostatic and magnetic. Furthermore, this description works best in terms of the column approximation and for weak fields. If the fields are strong and rapidly varying, there will be an interplay between the phase components due to dynamical scattering. As the description stands, the crystalline phase terms can be highly dynamic if the other terms can be treated as a perturbation. The usefulness of splitting the electrostatic component into three terms (C, E and G) will hopefully become apparent in the following.

2.2. Crystalline phase

The phase term induced by the interaction with the crystalline lattice is the most familiar in electron microscopy and diffraction physics. The electrostatic potential, $V(\mathbf{r})$, of a crystal can be written:

$$V(\mathbf{r}) = \sum_{g} V_{g} e^{2\pi i \mathbf{g} \cdot \mathbf{r}} \tag{5}$$

where the Fourier components, V_g , have phases, ϕ_g^V . Here, we explicitly state that the origin of the real-space coordinate \mathbf{r} coincides with a point of symmetry in the unit cell. The incident electron will be scattered by this potential distribution and at the exit surface of the crystal will have a wave function described by Eq. (1) and has been exhaustively studied in the framework of kinematical and dynamical theory of diffraction. The essential result is that in general:

$$\phi_g^V \neq \phi_g^C \tag{6}$$

Much effort has been applied to retrieving the phases of the diffracted beams and to determine the atomic crystal structure but in the following, we are not interested in the configuration of atoms within the unit cell but the variations of the lattice from unit cell to unit cell. Crystalline phase will therefore be more of a hindrance than an aim.

In our description, the phase changes due to the mean inner potential, V_o , will be treated along with other electrostatic fields, E. The crystalline phases ϕ_o^C therefore assume a zero mean inner potential, i.e., $\phi_o^V = 0$, which in no way affects dynamical scattering calculations for perfect crystals except for a constant phase shift of all the beams. Note that this does not exclude dynamical effects producing phase changes in the transmitted beam, and as a consequence $\phi_o^C \neq 0$ [38]. A local change in composition would also produce a change in the crystalline phases, but the main effect will often concern geometric phase, G.

2.3. Electrostatic phase

As mentioned above, crystals have a mean inner potential V_o with respect to the vacuum (taken as zero). This produces a uniform phase change of the wave front of the fast electron, equivalent to adding a constant phase to the transmitted and scattered beams. As with crystalline potential, the mean inner potential (MIP) can vary as a function of position becoming $V_o(\mathbf{r})$ due to changes in composition or density (including absence of material). We can also anticipate that the mean inner potential will vary with strain, as the local density will change. Electrostatic and geometric phases will therefore be correlated to some extent. The correlation will nevertheless be small and indirect, as the mean inner potential is only affected by volume changes (and not by individual strain components).

External or internal electric fields will also have an associated electrical potential, $V_E(\mathbf{r})$, whose gradient is the electric field, **E**:

$$\mathbf{E} = -\nabla V_E(\mathbf{r}) \tag{7}$$

The total electrostatic potential, $V_E(\mathbf{r})$, will therefore be the sum of these two terms:

$$V^{E}(\mathbf{r}) = V_{0}(\mathbf{r}) + V_{F}(\mathbf{r}) \tag{8}$$

For slowly varying electrostatic potentials (i.e. weak electric fields), the corresponding phase shift is obtained by integrating the potential along the path of the fast electron:

$$\phi^E = c_E \int V^E(\mathbf{r}) dz \tag{9}$$

with c_E the electron interaction constant given by

$$c_E = \frac{\pi}{\lambda E} \equiv \frac{2\pi}{\lambda} \frac{E_k + E_0}{E_k (E_k + 2E_0)} \tag{10}$$

where λ is the electron wavelength, E the total energy of the fast electron, which depends on the energy at rest E_0 and kinetic energy E_k determined by the accelerating voltage.

Naturally, Eq. (9) applies equally well to an infinitely thin crystal of electrostatic potential given by Eq. (5). The electric field could be external, placing the specimen between two electrodes, or internal due to an accumulation of charge or due to piezoelectricity of the sample. We have chosen to separate C and E because of these different physical origins. Placing electrostatic potentials for different atoms in the unit cell will create the crystalline potential $V(\mathbf{r})$ but will never recreate the piezoelectric effect. The other difference is that $V(\mathbf{r})$ is made of discrete periodicities, \mathbf{g} . We will assume that $V_0(\mathbf{r})$ and $V_E(\mathbf{r})$ are smoothly varying and on a length scale larger than the unit cell.

For most samples:

$$\phi_{g,0}^E = \phi^{MIP} \tag{11}$$

with the indicial notation indicating that the phase change will be the same for all beams, whether transmitted or diffracted.

2.4. Geometric phase

The originality of this description lies essentially with the geometric phase term and was the reason for explicitly dealing with the phases of the diffracted beams. Let us assume that the crystal has been bodily translated by a vector, \mathbf{u} :

$$\mathbf{r} \rightarrow \mathbf{r} - \mathbf{u}$$
 (12)

The wave function of Eq. (1) will become:

$$\psi(\mathbf{r} - \mathbf{u}) = \sum_{g} \psi_{g} e^{-2\pi i \mathbf{g} \cdot \mathbf{u}} e^{2\pi i \mathbf{g} \cdot \mathbf{r}}$$
(13)

The extra phase term induced by the crystal translation is given by

$$\phi_g^G = -2\pi \mathbf{g} \cdot \mathbf{u} \tag{14}$$

which is our definition for geometric phase. If our spatial origin in real-space is different to a symmetry point of the unit cell defined previously, all the diffracted beams will assume a phase shift. As previously, we will assume that this relation holds true for a varying displacement field:

$$\phi_{\sigma}^{G}(\mathbf{r}) = -2\pi \mathbf{g} \cdot \mathbf{u}(\mathbf{r}) \tag{15}$$

This equation is only strictly true for small displacement fields but large distortions can be treated by studying the phase gradients (and see later) [28].

Apart from distortion of the crystalline lattice due to strain, we shall consider that geometric phase also contains information about variations in local composition that can be described as a distortion of the basic lattice. Typically, this concerns compounds where a compositional variation produces a change in the lattice parameter without changing the crystal symmetry. The change in the complex

diffracted amplitude due to the different scattering potential will be incorporated into the crystalline amplitude and phase (C), and the mean inner potential in the electrostatic phase (E).

Take for example the case of fluctuations of germanium content in $\operatorname{Si}_x \operatorname{Ge}_{1-x}$ with mean composition SiGe as the reference lattice. The amplitude of the $(1\ 1\ 1)$ diffracted beam will vary with the local Ge concentration, and will be included in the amplitude $a_{111}^C(\mathbf{r})$. The distortion of the crystalline lattice will be described by $\phi_{111}^C(\mathbf{r})$ and any remaining phase changes by $\phi_{111}^C(\mathbf{r})$. Separating geometric phase from the crystalline and electrostatic phases will be important for the method in such cases.

2.5. Magnetic phase

For completeness, we include a description of the phase changes introduced by the presence of magnetic fields. The phase shift is given by

$$\phi^{M} = -\frac{e}{h} \int \mathbf{A}_{z}(\mathbf{r}) dz \tag{16}$$

where A is the magnetic vector field and z the direction of propagation. This magnetic field can result from an externally applied magnetic field or the magnetic field of the specimen. Given the definition of the magnetic vector potential:

$$\mathbf{B} = \nabla \wedge \mathbf{A} \tag{17}$$

the component of the magnetic field in the propagation direction does not produce a phase shift. From these relations, it can be shown that:

$$\int \mathbf{B}_{xy}(\mathbf{r})dz = \frac{\hbar}{e}(\hat{\mathbf{z}} \wedge \nabla \phi^{M})$$
(18)

where \mathbf{B}_{xy} is the component of the magnetic field in the xy-plane, and $\hat{\mathbf{z}}$ the unit vector in the propagation direction. In other words the iso-phase contours are equivalent to the magnetic field lines viewed in projection.

2.6. Dark-field electron holography (DFEH)

The geometric phase is only present in the diffracted beams and therefore cannot be measured by the conventional off-axis electron holography setup (Fig. 1a). It was in this context that dark-field electron holography was imagined [20] in complete independence to previous work [22]. The crystal is oriented in diffraction conditions for one of the lattice planes and the illumination conditions tilted so that the emerging diffracted beam is aligned with the optic axis, exactly as for conventional dark-field imaging, and an objective aperture applied to eliminate the other diffracted beams. A hologram is created from the interference between the diffracted beam emanating from an unstrained region of crystal, which serves as the reference, and a beam from the region of interest of strained crystal (see Fig. 1c). The relative phase of the diffracted beam between the two regions can then be determined from the dark-field hologram, assuming a suitable calibration of the carrier frequency. The darkfield holography configuration has an interesting advantage over the conventional setup. Assuming the specimen thickness is uniform, the amplitudes of the two beams, a_L and a_R , will be the same and therefore the holographic fringe contrast is maximised (see Eq. (1)).

To measure the geometric phase component, the other phase terms, notably crystalline and electrostatic phase, must be eliminated. To a first approximation, these two phases do not depend directly on the local strain. Therefore, if the sample is uniformly thick, these terms will cancel out and a direct measurement of geometric phase obtained. Indeed for the measurement of strain,

which depends on the phase gradient, it is only necessary that the gradient of the non-geometric phase terms be zero, or the gradient of the difference. Fortunately, the requirements for uniform thickness are not as stringent as for the measurement of dopant distributions since the geometric phase variations are generally quite large, as the examples will show. For the crystalline phase to be constant, the diffraction conditions must also be uniform over the two regions. Regions exhibiting bend contours should therefore be avoided.

The situation is more complex in the presence of compositional variations, as these will introduce additional crystalline and electrostatic phase terms. Significant and localised phase changes can occur at interfaces, which are therefore difficult to eliminate from the analysis (see later).

Finally, the measurement will provide the relative distortion of the reference lattice and the region of interest. Therefore, a strict mechanical strain analysis requires the reference region to be unstrained, otherwise a systematic error will arise. Note, that there is no fundamental reason why the reference region must be the same material as the region of interest, provided that it diffracts within the objective aperture. Only the interpretation requires a suitable adaptation. A common example is for an expitaxial strained layer of different composition to the substrate.

2.7. Bright-field electron holography

We will call the equivalent setup for the transmitted beam, the bright-field electron hologram (Fig. 1b). Here, the transmitted beam from the region of interest is interfered with that emanating from the reference region of crystal, and not with the beam in the vacuum as for the conventional setup (Fig. 1a). This configuration is of primary interest for assessing, and correcting the systematic errors of the dark-field measurements since for the transmitted beam, the geometric phase component should be zero (Eq. (14)).

3. Experimental details

Two test samples will be used to illustrate the technique, an array of dummy p-MOSFET transistors with embedded Si_{0.7}Ge_{0.3} sources and drains [20], and an etched silicon structure coated with a strained nitride layer [25]. TEM specimens are prepared by focussed ion beam (FIB) to a thickness of between 100 and 150 nm. Observations are carried out on the SACTEM-Toulouse, a Tecnai (FEI) 200 kV TEM equipped with a Cs corrector (CEOS), rotatable biprism and 2 k CCD camera (Gatan). Specimens were oriented close to a $[\overline{1} \ 10]$ zone axis. The microscope is operated in a pseudo-Lorentz mode using the corrector first transfer lens as a Lorentz lens and with the main objective lens and hexapoles switched off [39]. Typical fringe spacings are 1-2 nm, fringe visibilities of around 20%, and hologram widths from 300-500 nm allowing lengthwise fields of view of several microns. Strain fields are extracted using HoloDark 1.0 software developed in collaboration with HREM Research Inc. as a plugin for Digital-Micrograph (Gatan).

In principle, there is no restriction on the diffraction conditions. However, we have found that a Bragg condition on a systematic row, close to a zone axis is preferable for reasons which will be discussed later. Secondly, the biprism should be placed "within" the reference region, relative to the projected image, so that a region of the interference is produced between the reference, A, and part of itself, A' (Fig. 2a). This provides an internal reference within the hologram of the carrier frequency. This procedure avoids determining the carrier frequency from a subsequent conventional hologram, which is not always reliable.

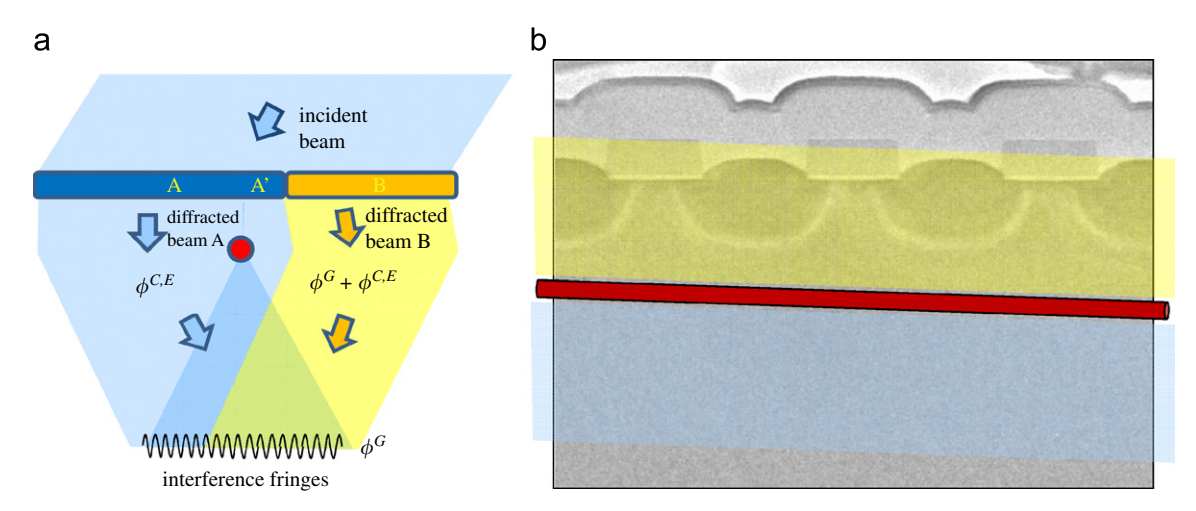


Fig. 2. Dark-field electron holography: (a) a diffracted beam from an unstrained region of crystal (in blue) is interfered with the same diffracted beam emanating from the region of interest (in yellow) with aid of biprism wire (red). Providing the crystal is of uniform thickness, the non-geometric phase terms cancel, or only produce a uniform phase change to a good first approximation, thus yielding the geometric phase component; (b) typical transistor geometry with reference zone in substrate and active region at the surface. (For interpretation of the references to color in this figure legend, the reader is referred to the web version of this article.)

A typical example for these two regions would be the substrate (A,A') and an active region of a device (B) (Fig. 2b). Note that the orientation of the biprism is unrelated to the direction of the diffraction vector. Its main function is to define the two regions and is generally placed to maximise the field of view.

3.1. Reconstruction method

Once the hologram is recorded the geometric phase can be retrieved. The procedure we use is based on the Fourier transform and necessitates the correct choice of side band, which can be understood using Fig. 3. The crystal diffracts into the transmitted beam, O, and diffracted beams from the undistorted crystal, A and A', and the strained region of crystal, B. The objective aperture is used to select only these diffracted beams. The biprism deflects these beams depending on whether they pass to the left (A) or the right (A',B). The relative deflection is denoted by \mathbf{q}_{c} , the carrier frequency. In this example, the voltage of the biprism is positive and is placed before the image plane. As usual, the Fourier transform of the holographic fringes will have two side bands. It can be seen that the direction of $\Delta \mathbf{g}$, the difference in reciprocal lattice vector, is unaltered in the side band pointing towards the substrate. It is this side band that we choose to reconstruct. Using the other side band simply changes the sign.

It is interesting to note that in this example, the region of crystal (B) with the smaller lattice spacing produced fringes (A–B) of a wider spacing than the reference region (A–A′). Indeed, this is the preferable condition to increase precision. Results with the ${\bf g}$ and ${\bf -g}$ diffracted beam will not therefore be identical from a practical point of view for the same biprism conditions.

The reference region of phase, A–A′, can be conveniently used to define both the unstrained state and the carrier frequency. Any phase gradients elsewhere in the hologram indicate a difference in local lattice parameter or orientation, as for geometric phase analysis. One important difference with GPA of HRTEM images, is that there is no internal reference for the undistorted lattice spacing, \mathbf{g} . To determine the g-vector in image coordinates, the corresponding lattice spacing, d_g , needs to be known along with the magnification of the hologram and the direction of the diffraction vector with respect to the image. This is not necessarily trivial, as our measurements are carried out in free-lens Lorentz mode. Careful attention therefore needs to be paid to calibrating magnification and rotations between diffraction and image planes. Alternatively, image features can provide internal

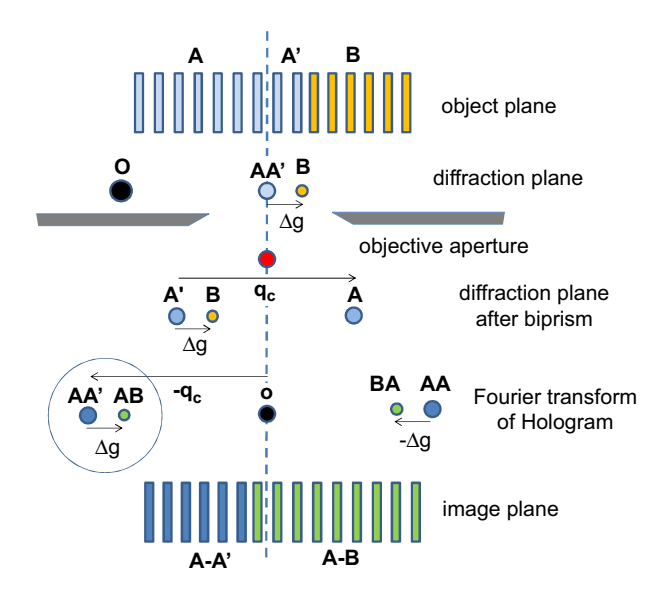


Fig. 3. Side-band selection for dark-field holography. See text for details.

calibration (for example, the spacing between devices) or recognisable crystallographic directions (for example, surface normals, or growth directions). The biggest error is to mistake the direction of **g**, which will invert the sign of the results and make compressive strain seem like a region of tensile strain, or vice-versa.

3.2. Strain tensor

The strain in the direction of the diffracting vector **g**, can be determined directly from the gradient of the phase [28]:

$$\overrightarrow{\Delta g} = \frac{1}{2\pi} \rightarrow \phi_g^G \tag{19}$$

Indeed, as for geometric phase analysis, this equation is more accurate than the interpretation in terms of displacement (Eq. (15)). The difference in reciprocal lattice vector, $\Delta \mathbf{g}$, can be determined unambiguously from the hologram but to determine percentage changes in lattice parameter and orientation the length and direction of \mathbf{g} is required, as discussed above. Using the (2 2 0) diffracted beam in the (0 0 1) grown strained-silicon

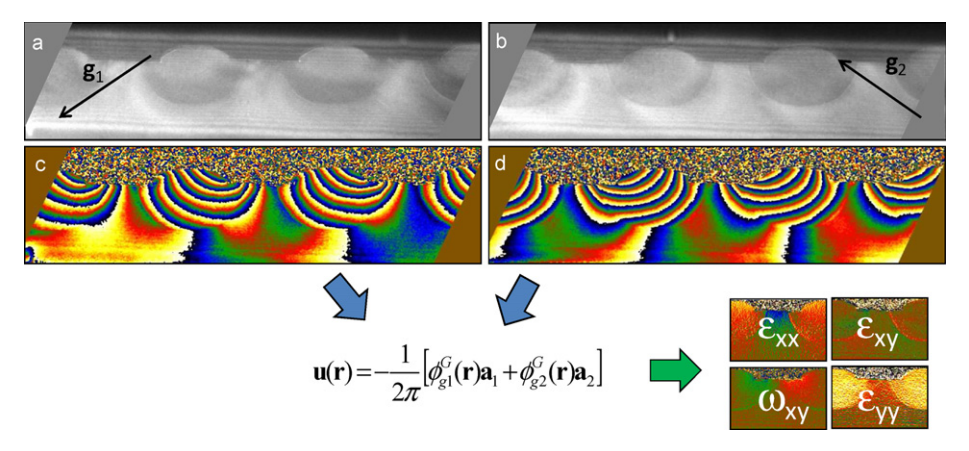


Fig. 4. Strain tensor mapping for a strained-silicon p-MOSFET transistor: (a) dark-field hologram from $\mathbf{g}_1 = (-1 - 1 - 1)$ diffracted beam; (b) dark-field electron hologram from $\mathbf{g}_2 = (-1 - 1)$ diffracted beam; (c) (-1 - 1 - 1) phase; (d) (-1 - 1) phase; (e) 2D displacement calculation and corresponding strain tensor components.

transistor example, the strain could be measured in the direction parallel to the specimen surface from source to drain [20].

To determine the 2D strain tensor, holograms need to be taken for two non-collinear diffraction vectors, $\mathbf{g_1}$ and $\mathbf{g_2}$. For the [1 1 0] zone-axis samples, we typically choose two {1 1 1} diffracted beams. The result from the experiment is shown in Fig. 4. The results can then be combined to determine the full in-plane strain tensor, ε_{ij} , and rigid-body rotation, ω_{ij} [20]. The difficulty with respect to HRTEM image analysis is that the holograms need to be aligned correctly. There is always some specimen or image shift between the two holograms, especially since we slightly reorient the crystal to a new diffraction condition between exposures. Fortunately, this alignment procedure is facilitated in that the technique is a medium-resolution technique. We either use the phase images or the amplitude images to identify equivalent sample areas. Ironically, uniform layer samples are therefore more of a challenge than devices.

4. Analysis

The technique has a number of advantages over geometric phase analysis of HRTEM images for the study of similar transistors [40]. The specimens do not need to be as thin, being more like those of conventional TEM. Specimens are therefore easier to prepare and the effects of thin-film relaxation reduced. The holographic interference fringes are much more stable than those of HRTEM images, which are highly sensitive to defocus, thickness and compositional changes. The major advantage, however, is the ability to analyse large regions of crystal at relatively low resolution. Furthermore, the sources of error are much easier to apprehend.

4.1. Precision

Random errors limit the precision of the measurements, some of which are inherent to off-axis holography and others that are more specific to dark-field holography. They are caused by the electron source, the specimen (thickness, amorphous layers, uniformity and contamination), and the detector. Consider the random errors in measuring the phase, and phase gradients, from an electron hologram. These will be influenced by the fringe contrast and the mean number of electrons forming the image. The mean intensity is determined by the diffracted intensity, the exposure time and quantum efficiency of the detector. The factor specific to dark-field holography is that the diffracted intensity needs to be maximised.

We choose, therefore, to align the specimen in such a way as to reproduce 2-beam conditions as closely as possible for the diffracted beam of interest. For the exact Bragg condition, the ideal thickness is then $(n+(1/2))\xi_g$, where n is an integer and ξ_g the extinction distance. For other thicknesses, the effective extinction distance can be modified by tilting slightly away from the Bragg condition, a common procedure in conventional darkfield imaging. Following the same logic, it is usually beneficial to acquire dark-field holograms with the $\{1\ 1\ 1\}$ diffracted beams instead of the $\{0\ 0\ 4\}$ beams, which are generally less intense, even if the higher-order beams are more sensitive to strain (see Eq. (15)).

The fringe contrast depends on the spatial coherence of the illumination conditions, the modulation transfer function (MTF) of the detector, the biprism stability, the mask used in Fourier space, the relative amplitude of the two interfering beams and the specimen stability. The latter, however, is a limited problem compared with HRTEM given the spatial frequencies involved (typically less than 0.5 nm⁻¹ in the Lorentz mode). The spatial coherence and the incident intensity are linked by the brightness of the electron source. The only specificity of dark-field electron holography with respect to conventional off-axis holography is that the amplitudes of the two interfered beams will be nearly identical, leading to maximal fringe visibility as mentioned previously.

Regarding the specimen, amorphous layers on the top and bottom surface of the sample, imperfections within the crystal, and contamination will produce "noise" in the phase image. Apart from improving the specimen preparation, this can be minimised by choosing the same size of objective aperture as the mask used in the Fourier analysis. Unuseful diffuse scattering will not then contribute to the background intensity. Indeed, this is a recommendation that we can make for conventional medium-resolution holography.

For an estimation of the precision, we measure the standard deviations of the strain measurements within a region of the reference (A–A′). Reducing the mask radius in the Fourier analysis will increase the precision, but at the expense of spatial resolution.

4.2. Spatial resolution

Technically, the spatial resolution of the reconstruction is determined by the radius of the Fourier mask used in the processing as this excludes spatial frequencies above a certain value. The maximum this can reasonably be is twice the holographic fringe spacing. For a given mask radius, finer fringe spacings will not improve the spatial resolution. More importantly, the spatial

resolution of the actual strain information is the ultimate limit. This is determined by the transfer function of the objective (Lorentz) lens, damping higher resolution details, and the specimen stability (drift and vibration) which will do likewise. An additional factor that degrades spatial resolution is the use of Bragg conditions rather than zone-axis orientations. Most interfaces will therefore be inclined when viewed in projection. However, the corresponding blurring is typically smaller than the above mentioned factors. The overall spatial resolution of our setup is about 2.5 nm, so there is no point in interpreting strain measurements on a smaller scale.

4.3. Systematic errors

Systematic errors in conventional off-axis holography are caused by the Fresnel fringes and geometrical distortions from the projector lens system of the microscope and the detector itself. The latter two influence the measurements exactly as for HRTEM and can be corrected for in the same way [41]. The Fresnel fringes are inherent to off-axis holography with a single biprism and can be removed to some extent by Fourier filtering. The best method is to use multiple biprisms to produce holograms without the Fresnel fringes in the first place [42].

More specific to dark-field holography is that the crystalline phase is not necessarily uniform across the measurement area (see Eq. (4)). This can be due to a change in thickness, specimen composition, diffraction conditions (specimen bending) or strain. The degree of tilting can be estimated from any bend contours that might be present. Similarly, the electrostatic, or most frequently the mean inner potential term, needs to be uniform. It is encouraging to note that the geometric phase is very large (several multiples of 2π , see e.g., Fig. 4) compared with the phase changes for dopant profiling (of the order of $\pi/6$, see e.g., Ref. [12]). Dark-field holography benefits therefore directly from the efforts made in that field to control specimen preparation, whilst at the same time having fewer requirements.

However well we measure the strain state of the thinned specimen, this is not identical to that of the bulk sample. As is well known, thin-film relaxation will occur at the two free surfaces [43]. The magnitude of this effect depends on the aspect ratio of the strained area to the specimen thickness. Measuring the strain in a narrow transistor channel will therefore be closer to the bulk value than for a wider gate length. The option we have chosen is to systematically perform finite-element method (FEM) modelling of the thin and bulk samples to estimate, and correct for, the error introduced by thin-film relaxation [20,23–25].

5. Corrections

5.1. Quantifying systematic errors

Systematic errors in the analysis can be apprehended in different ways, the most obvious being to verify that the measured strain is indeed on an average zero in the reference region A–A′ and that no systematic variations are visible. Another way is to compare two independent measurements, for example using different diffracted beams. Continuing the transistor example, the phase was also determined for the $(2\ 2\ 0)$ diffracted beam (Fig. 5a). This phase was compared with the equivalent phase calculated from the previously shown $(-1\ -1\ 1)$ and $(-1\ -1\ 1)$ phases (i.e., $-\phi_{g1}-\phi_{g2}$) (Fig. 5c).

The most pronounced effect is at the interface between the Si substrate and the embedded regions of SiGe where a phase jump is clearly visible in the reconstructed phase (Fig. 5c) and in the phase difference (Fig. 5e). It is natural that the crystalline phase and electrostatic phase be different between the two materials. Interpreting the strain determined at such an interface is therefore hazardous. The phase gradient within the SiGe in the phase difference (Fig. 5e), is probably due to a difference in the crystalline phases between the {1 1 1} and the (2 2 0) diffracted beams. We can estimate the systematic error in the strain from the

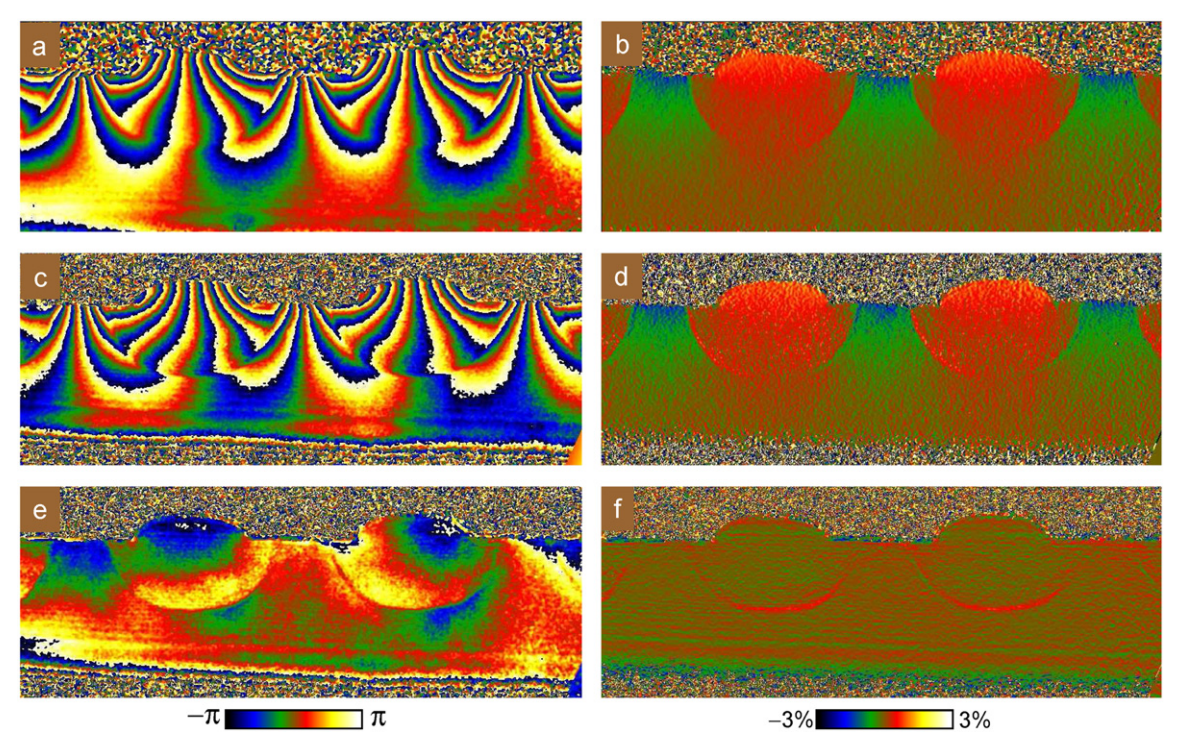


Fig. 5. Analysing systematic errors in dark-field holography: (a) phase of $(2\,2\,0)$ dark-field hologram; (b) corresponding $(2\,2\,0)$ strain; (c) equivalent $(2\,2\,0)$ phase calculated from $(-1\,-1\,-1)$ and $(-1\,-1\,1)$ hologram phases; (d) corresponding $(2\,2\,0)$ strain; (e) phase difference of (a)-(c); (f) strain difference of (b)-(d).

deformation map (Fig. 5f) to be 10^{-4} within the SiGe. This was determined from the average deformation measured in the island with respect to the substrate. In fact, for this case, the main systematic error is in the rotation, since the phase gradient is mainly perpendicular to the [2 2 0] direction.

5.2. Correcting thickness variations

Fig. 6 shows a test structure for the study of stress liners consisting of a comb-like periodical array of etched silicon trenches a few hundred nanometres deep and about 50–100 nm wide [25]. The Si is covered by a capping layer (CESL) of a few tens of nanometres thick of silicon nitride followed by silicon oxide. The processing results in a high level of stress in the nitride layer, which in turn deforms the silicon. The microscopy specimen was prepared by FIB and shadowing effects are visibly etched into the substrate (see Fig. 6a). These localised thickness changes will affect the phase measurements.

A dark-field hologram obtained using a (1 1 1) diffracted beam is shown in Fig. 6b. It shows the characteristic feature of a dark-field hologram in that there are no interference fringes in the vacuum (see inset), excepting the Fresnel fringes from the biprism. The hologram is analysed as usual by masking the side band in Fourier space which points towards the substrate to produce the phase (Fig. 6c) and amplitude maps (Fig. 6d). The deformation and rotation of the (1 1 1) lattice planes is determined directly by numerical differentiation of the phase (Fig. 6e and f). The artefacts from the specimen preparation can be clearly seen in the substrate in the phase and deformation maps. High-frequency artefacts are also present from the Fresnel fringes as vertical oscillations.

According to the theory, the transmitted beam should not contain any geometric phase components but only the crystalline and electrostatic phases. Indeed, the electrostatic phase should be the same for the transmitted and diffracted beams. We therefore can propose a correction procedure for thickness variations such as the ones shown. The idea is to acquire a bright-field hologram for the same diffraction conditions as the dark-field hologram and

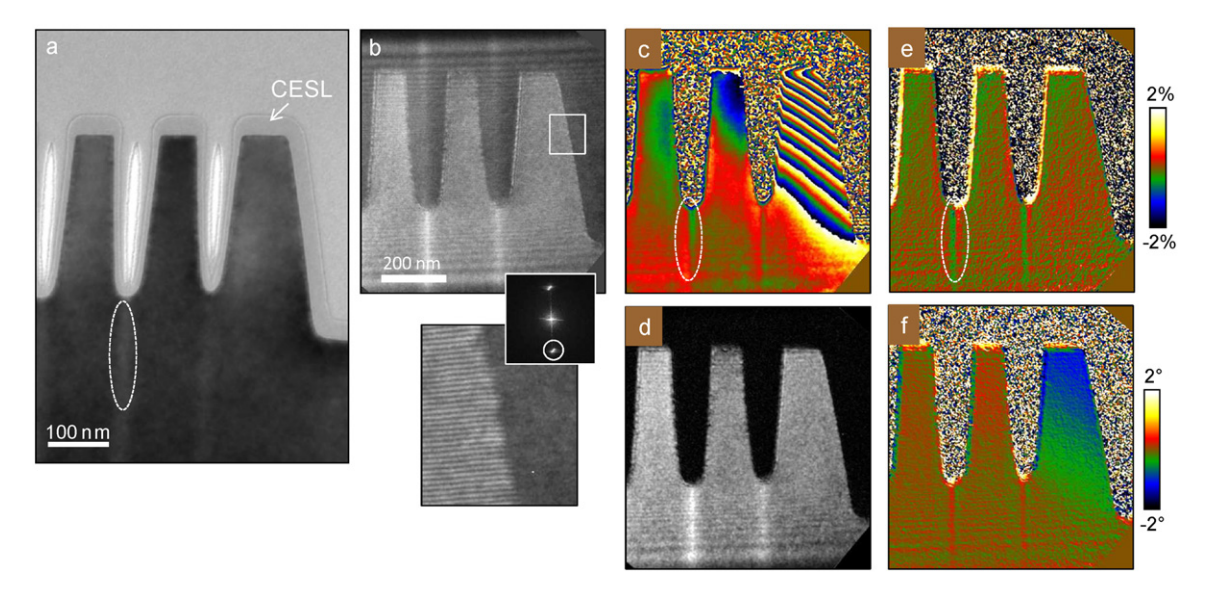


Fig. 6. Dark-field holography of a strained-Si test structure with stress liners (CESL): (a) conventional bright-field image, FIB shadowing marked; (b) dark-field hologram from (1 1 1) diffracted beam, Fourier transform and zoom inset; (c) phase; (d) amplitude; (e) local variation in planar spacing; (f) local lattice plane rotation.

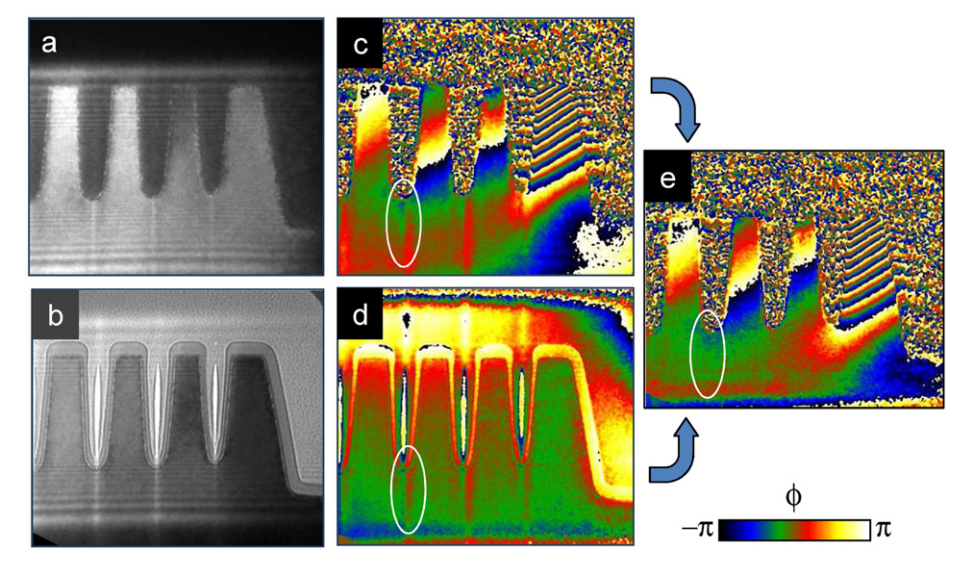


Fig. 7. Correction of thickness artefacts: (a) dark-field electron hologram; (b) bright-field hologram; (c) dark-field phase; (d) bright-field phase; (e) subtraction of the dark-field and bright-field phases. Ovals indicate principle artefacts. The Fresnel fringes have been removed by Fourier filtering.

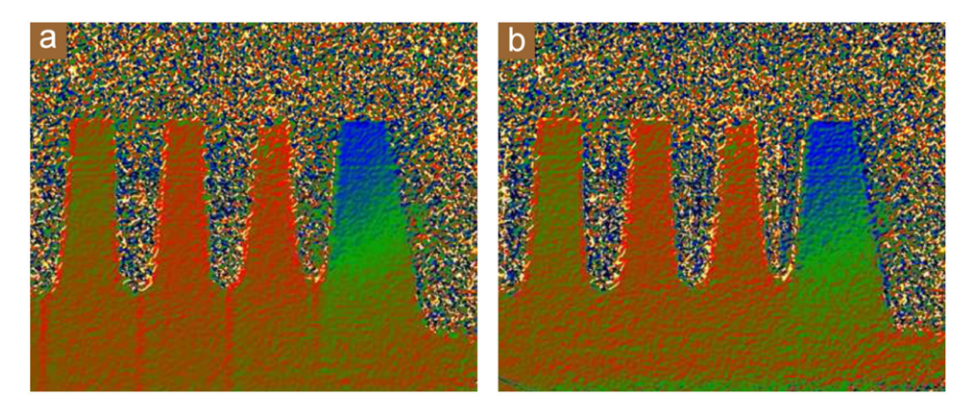


Fig. 8. Rigid-body rotation maps before (a) and after (b) removal of the thickness variation artefacts. The Fresnel fringe artefacts have also been removed from (b) by Fourier filtering.

subtract the two resulting phase images. The phase term from the mean inner potential should cancel.

To test this procedure a bright-field holograms was taken of the same area of the sample in a repeat experiment (Fig. 7b). Fig. 7e shows the result of the subtraction of the dark-field phase (Fig. 7c) and the bright-field phase (Fig. 7d). It can be seen that the artefacts due to the thickness variations have been successfully removed, and is confirmed by the rotation maps (Fig. 8). For this example we have also removed the Fresnel fringe artefacts by Fourier filtering.

6. Conclusions

Geometric phase can be placed in a theoretical framework regrouping measurements of electrostatic, magnetic and crystalline phases. This allows the identification of errors, both systematic and random, and suggests ways of correction and measurement such as the use of bright-field holograms. The dark-field electron holography technique is most reliable under uniform diffraction conditions, preferably close to a two-beam Bragg condition, and ultimately depends on the quality of sample preparation. Further theoretical work is required to better quantify the different random and systematic errors. On the experimental side, future improvements include the development of brighter electron sources to enlarge the fields of view and increase precision, sample preparation to limit sample bending, and aberration-corrected Lorentz modes to increase spatial resolution.

Acknowledgements

This work was supported by the European Commission through the ESTEEM project (Enabling Science and Technology through European Electron Microscopy, Grant no. IP3:0260019), the French Government (MINEFI) through the NANO2012 initiative (project CONTRAINTES), and by the French National Agency (ANR) in the frame of its program in Nanosciences and Nanotechnologies (HD STRAIN Project No. ANR-08-NANO-0 32). Laurent Clément and Pierre Morin (STMicroelectronics) are gratefully acknowledged for supplying the device material.

References

- [1] D. Gabor, A new microscopic principle, Nature 161 (1948) 777-778.
- [2] H. Lichte, Electron holography approaching atomic resolution, Ultramicroscopy 20 (1986) 293–304.
- [3] A. Orchowski, W.D. Rau, H. Lichte, Electron holography surmounts resolution limit of electron microscopy, Phys. Rev. Lett. 74 (1995) 399–402.

- [4] A. Tonomura, T. Matsuda, R. Suzuki, A. Fukuhara, N. Osakabe, H. Umezaki, J. Endo, K. Shinagawa, Y. Sugita, H. Fujiwara, Observation of Aharonov-Bohm effect by electron holography, Phys. Rev. Lett. 48 (1982) 1443–1446.
- [5] A. Tonomura, Electron-holographic interference microscopy, Adv. Phys. 41 (1992) 59–103.
- [6] R.E. Dunin-Borkowski, M.R. McCartney, D.J. Smith, S.S.P. Parkin, Towards quantitative electron holography of magnetic thin films using in situ magnetization reversal, Ultramicroscopy 74 (1998) 61–73.
- [7] M. Beleggia, T. Kasama, R.E. Dunin-Borkowski, The quantitative measurement of magnetic moments from phase images of nanoparticles and nanostructures—I. Fundamentals, Ultramicroscopy 110 (2010) 425–432.
- [8] M.J. Hÿtch, R.E. Dunin-Borkowski, M.R. Scheinfein, J. Moulin, C. Duhamel, F. Mazaleyrat, Y. Champion, Vortex flux channelling in magnetic nanoparticle chains, Phys. Rev. Lett. 91 (2003) 257207.
- [9] E. Snoeck, C. Gatel, L.M. Lacroix, T. Blon, S. Lachaize, J. Carrey, M. Respaud, B. Chaudret, Mangetic configurations of 30 nm iron nanocubes studied by electron holography, Nano Lett. 8 (2008) 4293–4298.
- [10] A. Gajdardziska-Josifovska, M.R. McCartney, W.J. De Ruijter, D.J. Smith, J.K. Weiss, J.M. Zuo, Accurate measurements of mean-inner potential of crystal wedges using digital electron holograms, Ultramicroscopy 50 (1993) 2017.
- [11] M.R. McCartney, D.J. Smith, R. Hull, J.C. Bean, E. Voelkl, B. Frost, Direct observation of potential distribution across Si–Si p–n junctions using off-axis electron holography, Appl. Phys. Lett. 65 (1994) 2603–2605.
- [12] W.D. Rau, P. Schwander, F.H. Baumann, W. Höppner, A. Ourmazd, Twodimensional mapping of the electrostatic potential in transistors by electron holography, Phys. Rev. Lett. 82 (1999) 2614–2617.
- [13] J. Cumings, A. Zettl, M.R. McCartney, J.C.H. Spence, Electron holography of field-emitting carbon nanotubes, Phys. Rev. Lett. 88 (2002) 056804.
- [14] A.C. Twitchett-Harrison, T.J.V. Yates, S.B. Newcomb, R.E. Dunin-Borkowski, P.A. Midgley, High-resolution three-dimensional mapping of semiconductor dopant potentials, Nano Lett. 7 (2007) 2020–2023.
- [15] P.A. Midgley, R.E. Dunin-Borkowski, Electron tomography and holography in materials science, Nat. Mater. 9 (2009) 271–280.
- [16] H. Lichte, M. Lehmann, Electron holography—basics and applications, Rep. Prog. Phys. 71 (2008) 16102.
- [17] M.R. McCartney, D.J. Smith, Electron holography: phase imaging with nanometer resolution, Annu. Rev. Mater. Res. 37 (2007) 729–767.
- [18] H. Lichte, D. Geiger, M. Linck, Off-axis electron holography in an aberrationcorrected transmission electron microscope, Phil. Trans. R. Soc. A 367 (2009) 3773–3793.
- [19] see papers in Ultramicroscopy 110, 2010, 375-572.
- [20] M.J. Hÿtch, F. Houdellier, F. Hüe, E. Snoeck, Nanoscale holographic interferometry for strain measurements in electronic devices, Nature 453 (2008) 1086–1089
- [21] M.J. Hÿtch, F. Houdellier, F. Hüe, E. Snoeck, Method, Device and System for Measuring Nanoscale Deformations. International Patent Pending No PCT/ FR2008/001302.
- [22] K.J. Hanszen, Methods of off-axis electron holography and investigations of the phase structure in crystals, J. Phys. D 19 (1986) 373.
- [23] F. Hüe, M.J. Hÿtch, F. Houdellier, H. Bender, A. Claverie, Strain mapping of tensiley strained silicon transistors with embedded $\mathrm{Si}_{1-y}\mathrm{Cy}$ source and drain by darkfield holography, Appl. Phys. Lett. 95 (2009) 073103.
- [24] J.M. Hartmann, L. Sanchez, W. Van Den Daele, A. Abbadie, L. Baud, R. Truche, E. Augendre, L. Clavelier, N. Cherkashin, M. Hytch, S. Cristoloveanu, Fabrication, structural and electrical properties of compressively strained Ge-oninsulator substrates, Semicond. Sci. Technol. 45 (2010) 075010.
- [25] M.J. Hÿtch, F. Hüe, F. Houdellier, E. Snoeck, A. Claverie, Strain metrology of devices by dark-field electron holography: a new technique for mapping 2D strain distributions, in: Proceedings of the International Electronic Device Meeting, IEDM, IEEE International, New York, 2009.

- [26] D. Cooper, J.-P. Barnes, J.-M. Hartmann, A. Béché, J.-L. Rouvière, Dark-field electron holography for quantitative strain measurements with nanometerscale spatial resolution, Appl. Phys. Lett. 95 (2009) 053501.
- [27] D. Cooper, A. Béché, J.-M. Hartmann, V. Carron, J.-L. Rouvière, Strain evolution during the silicidation of nanometer-scale SiGe semiconductors devices studied by dark-field electron holography, Appl. Phys. Lett. 96 (2010) 113508.
- [28] M.J. Hÿtch, E. Snoeck, R. Kilaas, Quantitative measurement of displacement and strain fields from HREM micrographs, Ultramicroscopy 74 (1998) 131–146.
- [29] A. Howie, M.J. Whelan, Diffraction contrast of electron microscope images of crystal lattice defects: development of a dynamical theory, Proc. Roy. Soc. London A 263 (1961) 217.
- [30] M.V. Berry, Quantal phase-factors accompanying adiabatic changes, Proc. Roy. Soc. London A 392 (1984) 45–57.
- [31] M.J. Hÿtch, F. Houdellier and E. Snoeck, Phase measurements: holography and geometric phase, in: Proceedings of the IMC16 International Microscopy Congress, Sapporo, 2006, vol. 2, p. 737.
- [32] C.T. Koch, V.B. Özdöl, P.A. van Aken, An efficient, simple, and precise way to map strain with nanometer resolution in semiconductor devices, Appl. Phys. Lett 96 (2010) 091901.
- [33] J.M. Cowley, Twenty forms of electron holography, Ultramicroscopy 41 (1992) 335–348.
- [34] C.T. Koch, A. Lubk, Off-axis and inline electron holography: a quantitative comparison, Ultramicroscopy 110 (2010) 460–471.

- [35] M.J. Hÿtch, T. Plamann, Imaging conditions for reliable measurement of displacement and strain from high-resolution electron microscope images, Ultramicroscopy 87 (2001) 199–212.
- [36] M.J. Hÿtch, Microsc. Microanal., Analysis of variations in structure from high resolution electron microscope images by combining real space and Fourier space information, Microstruct 8 (1997) 41–57.
- [37] M.J. Hÿtch, Phases in electron microscopy, Thèse d'Habilitation, Université de Toulouse, 2006.
- [38] A. Lubk, D. Wolf, H. Lichte, The effect of dynamical scattering in off-axis holographic mean inner potential and inelastic mean free path measurements, Ultramicroscopy 110 (2010) 438-446.
- [39] E. Snoeck, P. Hartel, H. Müller, M. Haider, P.C. Tiemeijer, Using a CEOS objective lens corrector as a pseudo Lorentz lens in a Tecnai F20 TEM, in: Proceedings of the IMC16 International Microscopy Congress, IMC, Sapporo, 2006, vol. 2, p. 730.
- [40] F. Hüe, M.J. Hÿtch, H. Bender, F. Houdellier, A. Claverie, Direct mapping of strain in a strained-silicon transistor by high-resolution electron microscopy, Phys. Rev. Lett. 100 (2008) 156602.
- [41] F. Hüe, C.L. Johnson, S. Lartigue-Korinek, G. Wang, P.R. Buseck, M.J. Hÿtch, Calibration of projector lens distortions, J. Electron Microsc. 54 (2005) 181–190.
- [42] K. Harada, A. Tonomura, Y. Togawa, T. Akashi, T. Matsuda, Double-biprism electron interferometry, Appl. Phys. Lett. 84 (2004) 3229–3231.
- [43] M.M.J. Treacy, J.M. Gibson, A. Howie, On elastic relaxation and long wavelength microstructures in spinodally decomposed In_xGa_{1-x}As_yP_{1-y} epitaxial layers, Phil. Mag. A 51 (1985) 389.